Applied Surface Science 630 (2023) 157357

Contents lists available at ScienceDirect

Applied Surface Science

journal homepage: www.elsevier.com/locate/apsusc

Full Length Article

Exalted dual-scale surface roughening in laser ablated aluminum capped with a transparent thin film: Wetting and anti-icing behavior

Ismail Ghemras [a,b,1], Laura Montes [c,1], Carmen Lopez-Santos [c,d,*], Agustin R. González-Elipe [c], Victor Rico [c,*]

[a] Centre de Développement des Technologies Avancées (CDTA), Cité 20 août 1956, Baba Hassen, BP : 17, DZ-16303 Algiers, Algeria
[b] Faculté de Physique, USTHB, BP 32 El-Alia, Algiers, Algeria
[c] Instituto de Ciencia de Materiales de Sevilla (CSIC-ICMSE. Sevilla), Avda. Américo Vespucio 49, 41092 Seville, Spain
[d] Departamento de Física Aplicada I (Universidad de Sevilla) Escuela Politécnica Superior, Virgen de Africa 41011, Seville, Spain

ARTICLE INFO

Keywords:
Laser Processing
Dual-scale surface roughening
Aluminum
Wetting
Anti-icing

ABSTRACT

Near infrared laser ablation of metals, specifically aluminum, has been systematically applied to generate surface roughness. Very high laser fluences may even lead to a so called "explosive" ablation regime where roughness becomes dramatically enhanced. In the present work we have developed an alternative methodology that, utilizing milder laser irradiation conditions (i.e. laser fluences from 0.37 to 0.72 J/cm^2), renders aluminum surfaces with a dual-scale roughness character and Sp parameter values twice or even trice the value found in reference samples. This has been possible for aluminum substrates coated with a highly transparent aluminum oxynitride capping layer. The resulting surfaces, consisting of very rough partially oxidized aluminum with negligible amounts of nitrogen species, resulted highly hydrophobic and depicted long icing delay times as required for anti-icing applications. A correlation has been found between the wetting and anti-icing behaviors, the use of a capping layer and the laser irradiation conditions. To account for this exalted roughening phenomenon, we propose that the transparent capping layer confines the laser energy within the aluminum shallow zones, delays the formation of the plasma plume and produces an enhancement in the aluminum ablation, even at relatively low laser fluences.

1. Introduction

Near infrared laser treatment of aluminum and other metals is a well-known procedure to modify their surface roughness and/or to induce other surface micro and nanostructuration phenomena [1–3]. This versatile surface engineering procedure has been widely utilized for the surface nanostructuration and roughening of a large variety of metals, aiming, among other applications, at enhancing hydrophobicity and increasing the freezing delay time, two features associated with water repellency and anti-icing behavior [4–9]. Roughness and final surface termination of laser treated metals are known to strongly depend on laser parameters such as repetition time, scanning rate or power [1–7]. For given high laser fluence operational conditions, ablation of certain metals like aluminum proceeds through a so-called "explosion" regime [10–14]. This produces highly rough surfaces, which may experience additional oxidation processes when the laser treatment is carried out in air. Different models and experimental and theoretical studies have been carried to account for the basic features of this explosive mechanism [10,15–17], whereby the accumulation of energy within the laser spot area plays a fundamental role.

Although fresh laser ablated metal surfaces are generally hydrophilic, it is known that upon air exposure for long enough time, contamination by airborne carbon species induces their transformation into hydrophobic or superhydrophobic states [6,9,18–20]. Depending on roughness characteristics, wetting behavior is commonly described by the Wenzel [21] and Cassie-Baxter [22] wetting models. The latter regime, known to render a superhydrophobic wetting state, commonly applies to surfaces depicting a dual scale roughness and air pockets in surface open pores [23–26]. Usually, this type of rough surfaces also presents a contrasted anti-icing response, which can be evidenced by long freezing delay times of water droplets placed onto the surface [4,9,23,25]. This behavior has been linked with the lack of surface sites

* Corresponding authors at: Instituto de Ciencia de Materiales de Sevilla (CSIC-ICMSE. Sevilla), Avda. Américo Vespucio 49, 41092 Seville, Spain (C. Lopez-Santos).
E-mail addresses: mclopez@icmse.csic.es (C. Lopez-Santos), victor@icmse.csic.es (V. Rico).
[1] These coauthors contributed equivalently.

https://doi.org/10.1016/j.apsusc.2023.157357
Received 22 February 2023; Received in revised form 14 April 2023; Accepted 21 April 2023
Available online 25 April 2023

with the critical size required for ice nucleation at minus zero temperatures [23,27–29].

Focusing in the development of an effective surface engineering method to make metal surfaces water and ice repellent, the present work discloses an alternative laser-based ablation procedure for the surface roughening of aluminum at relatively low laser fluences. It consists of the near infrared (NIR) laser irradiation of an aluminum plate covered with a highly transparent aluminum oxynitride thin film prepared by magnetron sputtering [30–33]. The choice of an amorphous aluminum oxynitride as capping layer instead of pure aluminum oxide or nitride cope with the requirements of room temperature deposition in order to do not affect the aluminum substrates (crystalline AlN thin films are prepared at high temperatures [34–36]) and a high UV–vis-NIR transparency, meanwhile the nitrogen atoms of the coatings may serve as witness of an efficient removal of the capping layer during the ablation process.

Outstandingly, the roughest surfaces obtained by the outlined procedure approach the roughness of laser ablated aluminum substrates subjected to more extreme conditions [10–14], even if the herein utilized fluences are smaller than those reported for "explosive" processes [10–17]. It is also realized that the transparent aluminum oxynitride capping layer hinders, but not prevent the aluminum ablation and the almost complete removal of the oxynitride capping layer. It is also shown that modulating the laser irradiation conditions permits tailoring the surface roughness in such a way that, depending on roughness characteristics and its dual-scale character, superhydrophobicity and very long freezing delay times may be achieved as expected for a Cassie Baxter wetting state.

2. Experimental

2.1. Oxynitride thin film preparation

Aluminum oxynitride thin films have been prepared by magnetron sputtering from a pure aluminum target of 3 in. of diameter. The power source was operated in pulsed DC mode at 80 kHz, 40% duty cycle, and a power varying from 100 to 200 W. As nonreactive gas, a flow of Ar of 10 sccm was dosed into the chamber, leading to a working pressure of 0.15 Pa. A nitrogen flow was set at 6 or 8 sccm. Base vacuum pressure before deposition was in the order of 10^{-4} Pa. The amount of N_2 gas introduced in the discharge, the distance sample-target (22 cm) and the power applied to the target served as control parameters of the film stoichiometry. Table 1 summarizes the selected deposition conditions for samples denoted as A to D. Typical deposition rates of 10 nm/min were obtained for the utilized deposition conditions.

2.2. Laser ablation experiments

Experiments have been carried out with Al6061 surface-polished substrate pieces (15 mm × 15 mm size) (Goodfellow). These pieces were cleaned by rinsing in detergent water solutions prior to the deposition of the capping layer and the laser ablation treatments. Laser irradiation was carried out for specimen without and with the aluminum oxynitride coating acting as capping layer placed in a vacuum chamber. This chamber is described in the supporting information section, together with additional details of the irradiation (See supporting information S1, Fig. S1 and additional explanations). Table 2 summarizes the selected irradiation conditions. Samples have been designated as L1, L2, L3 and L4 or $L1_{cl}$, $L2_{cl}$, $L3_{cl}$ and $L4_{cl}$ (cl for "capping layer"), for samples resulting from laser irradiation conditions 1 to 4, either for a bare aluminum substrate (L1-L4) or for this substrate covered with an aluminum oxynitride coating ($L1_{cl}$-$L4_{cl}$), respectively.

Table 1
Summary of preparation conditions used to deposit the aluminum oxynitride films and some basic optical characterization parameters.

Sample	Power (W)	Flow of N_2 (sccm)	Refractive index	Absorption Edge (eV)
A	100	6	1.75	3.82
B	100	8	1.71	3.79
C	150	8	1.93	4.07
D	200	8	1.89	3.92

2.3. Characterization of thin films and ablated samples

The oxynitride thin films were simultaneously deposited onto bare aluminum substrates and, for specific characterization tests, also on a silica plate and a silicon wafer. The thin films deposited on silica were optically characterized by transmission UV–vis-NIR spectroscopy in a Perking Elmer Lambda 750 S apparatus. Surface planarity, compactness, cross section thickness and microstructure of the thin films deposited onto the silicon wafer were characterized by Scanning Electron Microscopy (SEM) with a HITACHI S4800 field emission microscope working at 2 kV and 10 mA. Typical thickness of the films covering the aluminum substrates for the laser ablation experiments was 1 μm. Top-view SEM micrographs were also taken to characterize the surface state of ablated samples.

Confocal microscopy analysis of ablated samples was carried out with a ZEISS LSM 7 DUO microscope in the CITIUS of the University of Seville. Roughness parameters were calculated from the confocal surface images over an area of 250 μm × 350 μm. Two roughness parameters have been determined, i.e., Sq, defined as the medium quadratic height and calculated according to $S_q = \sqrt{\frac{1}{n\sum_{i=1}^{n} yy_i}}$ and Sp, defined as the average of the maximum height of the peaks in the area of study, both expressed in microns. Usually Sp is higher than Sq and is significantly affected if roughness distribution is not homogeneous or protuberances and high asperities appear in the examined area.

Surface analysis of the oxynitride films and ablated samples was carried out by X-ray Photoelectron Spectroscopy (XPS) using the Al Kα radiation. Binding energy (BE) of spectra was calibrated with the C 1 s peak of the adventitious carbon present in all samples, taken at 284.5 eV.

Table 2
Summary of laser conditions utilized for the preparation of irradiated samples, resulting fluences and irradiances, values of roughness (Sp and Sq) parameters and estimation of final content of nitrogen in the ablated surfaces.

Sample	P, SR, PF (%, mm/s, kHz)[1]	Fluence (J/cm^2)	Irradiance (MW/cm^2)	Ratio N/Al[2]	Sq (um)	Sp (um)
S_{Cl}	Coating on glass	–	–	0.4–0.5	–	–
AI	–	–	–	–	0.9 ± 0.3	8.8 ± 0.8
Al_{Cl}	Coating Al 6061	–	–	0.4–0.5	0.6 ± 0.2	8.8 ± 0.3
L1	20, 1000, 20	0.37	0.58	–	0.6 ± 0.1	5.2 ± 0.4
$L1_{cl}$	20, 1000, 20	0.37	0.58	0.06 ± 0.04	0.7 ± 0.3	18.6 ± 1.6
L2	40, 1000, 20	0.72	1.15	–	2.1 ± 0.2	13.0 ± 1.3
$L2_{cl}$	40, 1000, 20	0.72	1.15	0.1 ± 0.05	2.6 ± 0.2	35.3 ± 2.4
L3	20, 100, 20	0.37	5.73	–	0.9 ± 0.3	11.5 ± 0.7
$L3_{cl}$	20, 100, 20	0.37	5.73	~0	3.5 ± 0.5	24.7 ± 1.7
L4	40, 100, 20	0.72	11.46	–	3.2 ± 0.2	14.3 ± 1.0
$L4_{cl}$	40, 100, 20	0.72	11.46	~0	4.3 ± 0.1	22.3 ± 1.1

[1] P: % maximun laser power; SR: scan rate (mm/s); PF: pulse frequency (kHz).
[2] Atomic concentration ratio obtained from the XPS analysis of samples.

To ascertain the possible incorporation of oxygen from the air in the oxynitride capping layers, the analyzed samples were subjected to a mild Ar^+ sputtering cleaning treatment for about 1 min.

2.4. Wetting and freezing analysis

After laser ablation, samples were stored in air for a minimum time of one month to ensure the stabilization of their wetting behavior. Static, dynamic and sliding contact angles were determined by the Young method with a DataPhysics goniometer using droplets of 2 μL (for static WCA) and 5 μL (for dynamic wetting analysis to determine hysteresis contact angles, HCA) of deionized and bidistilled water (i.e., high-purity water). Rolling-off angles were determined with water droplets of different sizes, although the reported values for the capped and laser ablated samples were obtained with standard water droplets of 5, 10 and 15 μL. The determined WCA and HCA values are an average over five-seven measurements on each sample which means a margin of error of around 10%. An analysis of the possible transition from a Cassie-Baxter to a Wenzel wetting state as a function of the Laplace pressure of droplets has been done for the superhydrophobic surfaces varying the volume of the water droplets and measuring the WCA as a function of droplet size as reported in ref [37].

Freezing delay (FD) times were measured in a temperature-controlled chamber TFC100 assisted by a thermoelectric module, which has been reported in previous publications [9,23]. The freezing chamber was provided with lateral glass windows to follow the shape evolution of water droplets deposited onto the surface. Cooling system consisted of a Peltier of a size bigger than the sample area. Temperature was controlled and adjusted with a thermocouple placed onto the analyzed surface nearby the droplet. During the measurements the main source of ambient humidity in the chamber was the water vapor in equilibrium with the supercooled water droplets or the ice particles at −5°C (i.e., around 400 Pa [38]). A retractable syringe filled with water was used to drip 2 μL of water onto the surface of samples. The following cooling procedure was adopted for these tests: water was dripped onto the surface at 15 °C, then the substrate was fast cooled to − 5 °C. In all cases, a heterogeneous freezing was confirmed by the observation of the progression of an ice front from the solid − liquid interface toward the top of the droplet [27–29].

3. Results and discussion

3.1. Synthesis and characterization of aluminum oxy-nitride thin films

The fabricated capping layers were amorphous by X-ray diffraction to avoid any possible absorption/distortion of the laser beam, an optical effect which is reported to occur with crystalline AlN films characterized by a low second order absorption around the NIR wavelength of the utilized laser [39–41].

Table 1 shows a selection of investigated oxynitride samples (denoted A to D) with reference to the utilized deposition conditions and including a summary of basic optical characteristics determined from their UV–vis-NIR transmission spectra as explained below.

Fig. 1**a)** shows a cross section SEM micrograph of this type of thin films deposited onto a silicon wafer (the selected example corresponds to sample C in Table 1). This figure exemplifies the compact character of the columnar structure of these thin films, an important feature for the effective laser roughening of the capped aluminum substrates. An approximate capping layer thickness of 1 μm, as in the example in Fig. 1**a)**, was selected to cap the aluminum substrates for their laser treatment. The synthesized samples had different surface contents of nitrogen and oxygen as determined by XPS analysis. Since additional surface oxygen would likely be incorporated from the air, N/O ratio in the bulk of the film was estimated after a mild Ar^+ etching prior to the XPS analysis of sample. N/O ratios higher than one were obtained for thin films C and D, while this ratio was smaller for thin films A and B.

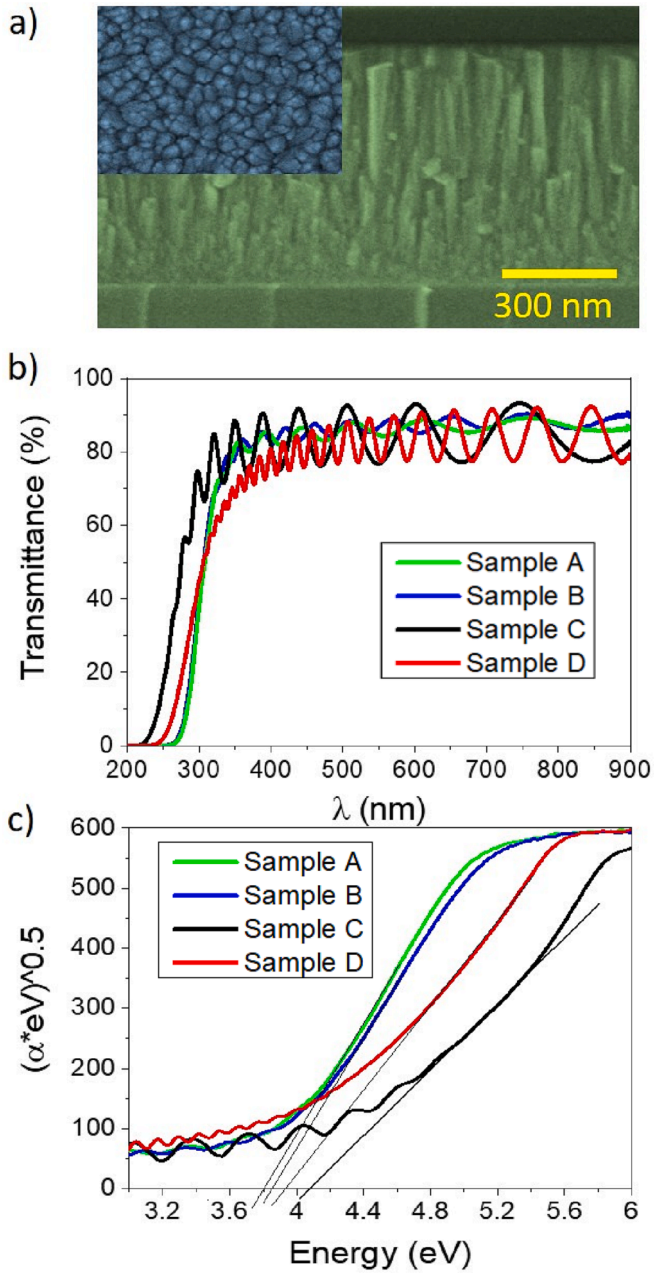

Fig. 1. Characterization analysis of the aluminum oxynitride thin films to select the most appropriate capping layer to cover the aluminum substrates. a) Cross section micrograph taken for sample C as example of the thin film microstructure (The top-view inset has the same size scale). b) series of UV–vis and close NIR transmission spectra recorded for selected oxynitride aluminum thin films (samples A-D) deposited onto a transparent silica substrate. c) Tauc plot to determine the absorption band edge of the selected thin film samples A-D.

The high transparency of the prepared oxynitride films both in the visible and, particularly in the NIR region of the spectra, is proved by the UV–vis-NIR transmission spectra reported in Fig. 1**b**) and in the supporting information **Fig. S2**), taken for thin films of different thicknesses from 500 nm to 1.5 μm deposited on a silica support. A Cauchy type fitting analysis of the interference oscillations of the spectra in Fig. 2**b)** was applied for a rough estimation of the refraction indexes of the films (see Table 1). The obtained values vary from 1.71 (sample B) to 1.93 (sample C), increase with the nitrogen content in the bulk of the films and are similar to those reported for other oxynitride films [30–33]. Fig. 1 **c)** shows the Tauc plots drawn to determine the absorption edge of

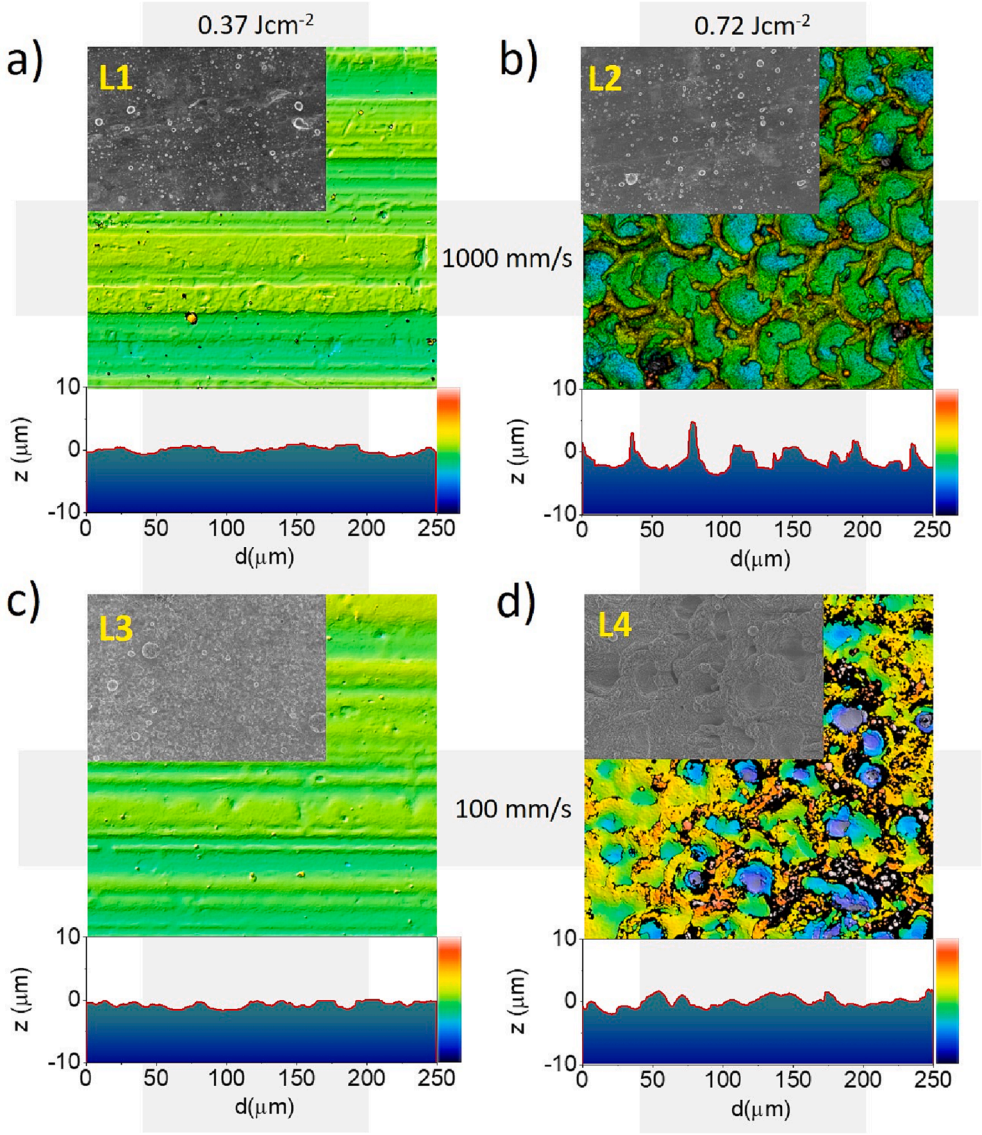

Fig. 2. a)-d). Top view sem micrographs and confocal microscopy images of samples L1-l4, resulting from the laser irradiation of bare aluminum substrates. linear profiles deduced from the confocal images of these samples are included to better illustrating their roughness characteristics. lateral size scales of sem and confocal images are the same than for the profile graphics.

the different thin films. The values determined for samples A-D are reported in Table 1. Absorption edges increase with the nitrogen content and are similar to those reported for other aluminum nitride and oxynitride thin films prepared by magnetron sputtering (MS) [30–33]. A maximum value of 4.1 eV was found for sample C. To carry out the laser ablation treatments of the aluminum coated samples, we selected as capping layer this oxynitride thin films, characterized by a high transmission in the visible and NIR regions of the spectrum, particularly at the laser wave-length of 1064 nm (see a spectrum of sample C recorded from 200 to 1500 nm in the supporting information **Fig. S2**).

3.2. Roughening of the capped aluminum substrates by NIR laser irradiation

NIR laser irradiation of aluminum is known to produce the roughening of its surface [5–9], a process that can be modified through the adjustment of the laser fluence. The SEM and confocal microscopy analysis of the bare aluminum substrates subjected to laser irradiation (samples L1-L4) are reported in Fig. 2. Sp and Sq roughness parameter values deduced from the analysis of confocal images of the laser treated aluminum substrates in this figure are included in Table 2 as a function of irradiation conditions. The table also includes data for the following reference samples: bare aluminum substrate (Al), this substrate covered with the capping layer (Al_{cl}) and the capping layer deposited on a silica plate (S_{cl}). An estimation of the residual content of nitrogen determined by XPS in the ablated capped samples is also included in the table in the form of the N/Al atomic ratio. The almost negligible amount of detected nitrogen in samples Ln_{cl} proves the effectiveness of the capping layer removal by laser irradiation.

According to Fig. 2 and the data in Table 2, samples L2 and L4, both of them prepared upon laser irradiation with a fluence of 0.72 J cm^{-2}, depict a significant increase in roughness, which is clearly evidenced by the assessment of the values of the two roughness parameters, Sp and Sq. Interestingly, sample L4, prepared with the highest irradiance, presented the higher roughness. Meanwhile, samples L1 and L3, prepared with a laser fluence of 0.37 J cm^{-2}, presented roughness parameters values that were similar or even smaller than that of the reference sample Al. This means that low fluence treatments may produce a flattening rather than a roughening the bare aluminum substrate surfaces.

A similar topography analysis of the surface of samples $L1_{cl}$-$L4_{cl}$ is

shown in Fig. 3. Roughness parameter values are gathered in Table 2. The images and line profiles in Fig. 3 reveal that sample $L1_{cl}$ obtained with a laser fluence of 0.37 J cm^{-2} is relatively flat at the nano- and micro-scales, although still rougher than sample L1, is evidenced by the values of the roughness parameters in Table 2. Interestingly, sample $L1_{cl}$ depicted a significant increase in the Sp parameter, which is more sensitive to large area topography fluctuations. Sample $L3_{cl}$ was obtained with the same laser fluence of 0.37 J cm^{-2}, but varying the scan rate in order to increase the irradiance (0.5 and 5.73 MW cm^{-2} for samples $L1_{cl}$ and $L3_{cl}$, respectively). Sample $L3_{cl}$ was rougher than $L1_{cl}$ (see Sp and Sq parameters in Table 2), and depicts a rather heterogenous surface morphology, characterized by a dual scale roughness topography where high aspect ratio asperities and nanofiber accumulations could be observed by top view SEM and confocal microscopy analysis (c.f. Fig. 3**c**)). The significant increase in the value of Sp of this sample can to be attributed to the surface protrusions observed over large areas. Meanwhile, an enlarge scale SEM micrograph analysis of this sample, **Fig. S3** in the supporting information section, confirms the formation of nanosized fiber-like structures at the surface (note however, that protrusions and nanofibers are not homogeneously distributed over the surface, making this sample surface quite heterogeneous).

Table 2 reveals that samples $L2_{cl}$ and $L4_{cl}$, obtained upon laser irradiation at the highest fluence, presented maximum roughness values, particularly sample $L4_{cl}$ (see its Sq parameter in this table), which was prepared using the maximum irradiance of the series. It is also quite significant in this table that samples Ln_{cl} are much rougher than the equivalent samples Ln. In other words, it appears that covering the aluminum with a transparent capping layer considerably enhances the laser induced roughening of the aluminum substrate beneath. We tentatively propose that the capping layer contributes to reduce the energy required for an effective substrate ablation to, eventually, approach an "explosive" regime [10–14]. Moreover, the quite effective surface ablation of samples Ln_{cl} produces the removal of their capping layer, as proved by the loss of most nitrogen from the surface in the ablated samples (c.f. see XPS results in Table 2). For example, sample $L1_{cl,}$ the one depicting the lowest surface roughness of the series (i.e., as resulting from a mild ablation impact), presented a very small N/Al atomic ratio of 0.06 as expected from an almost complete removal of the capping layer components for the used irradiation. Similar negligible nitrogen contents were also found for the other Ln_{cl} samples using higher fluences, proving an effective capping layer removal in all cases.

To further illustrate the chemical changes experienced by the surface of capped samples subjected to ablation, Fig. 4 shows the N1s, O1s and Al 2p spectra of sample $L2_{cl}$ before and after laser irradiation. Before

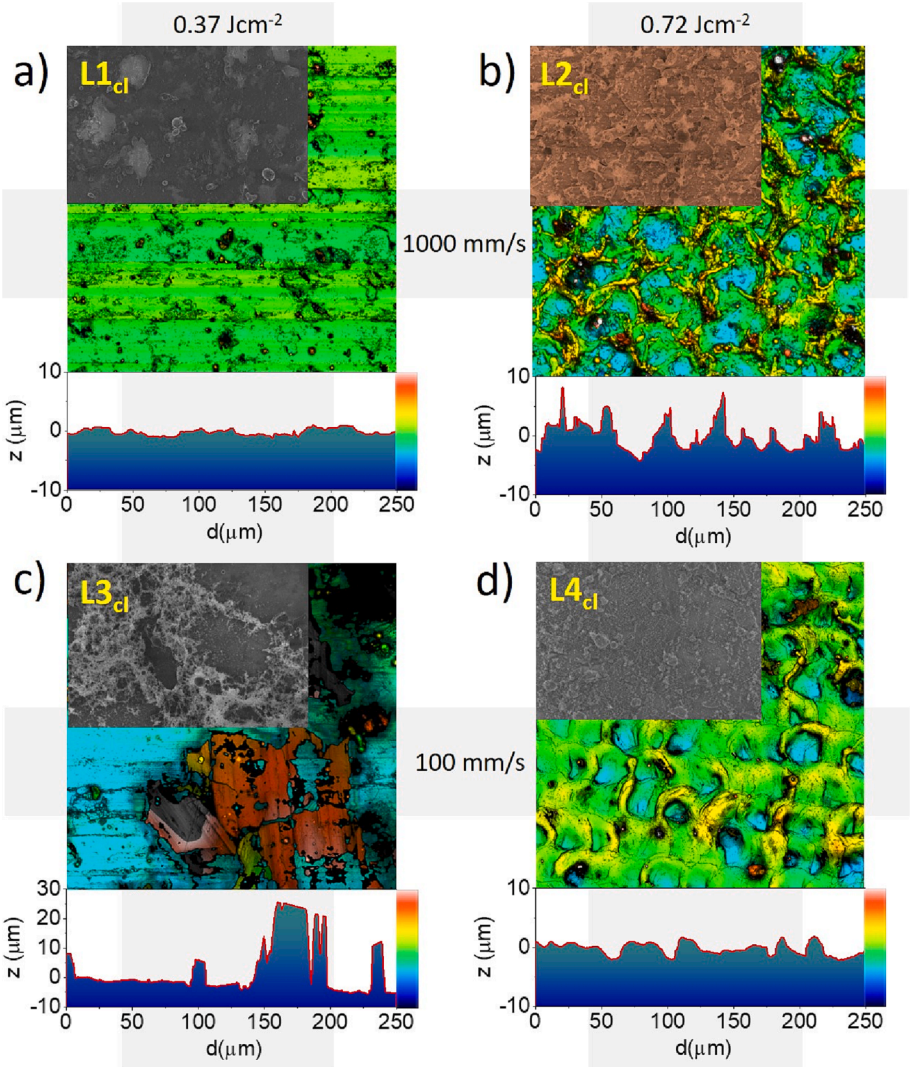

Fig. 3. a)-d). Top view sem micrographs and confocal microscopy images of samples $L1_{cl}$-$L4_{cl}$, resulting from the laser irradiation of the aluminum oxynitride capped aluminum substrates. Linear profiles deduced from the confocal images of these samples are included to better illustrate their roughness characteristics. Note the different y-scale of the linear profile plot in c). Lateral size scales of SEM and confocal images are the same than for the profile graphics.

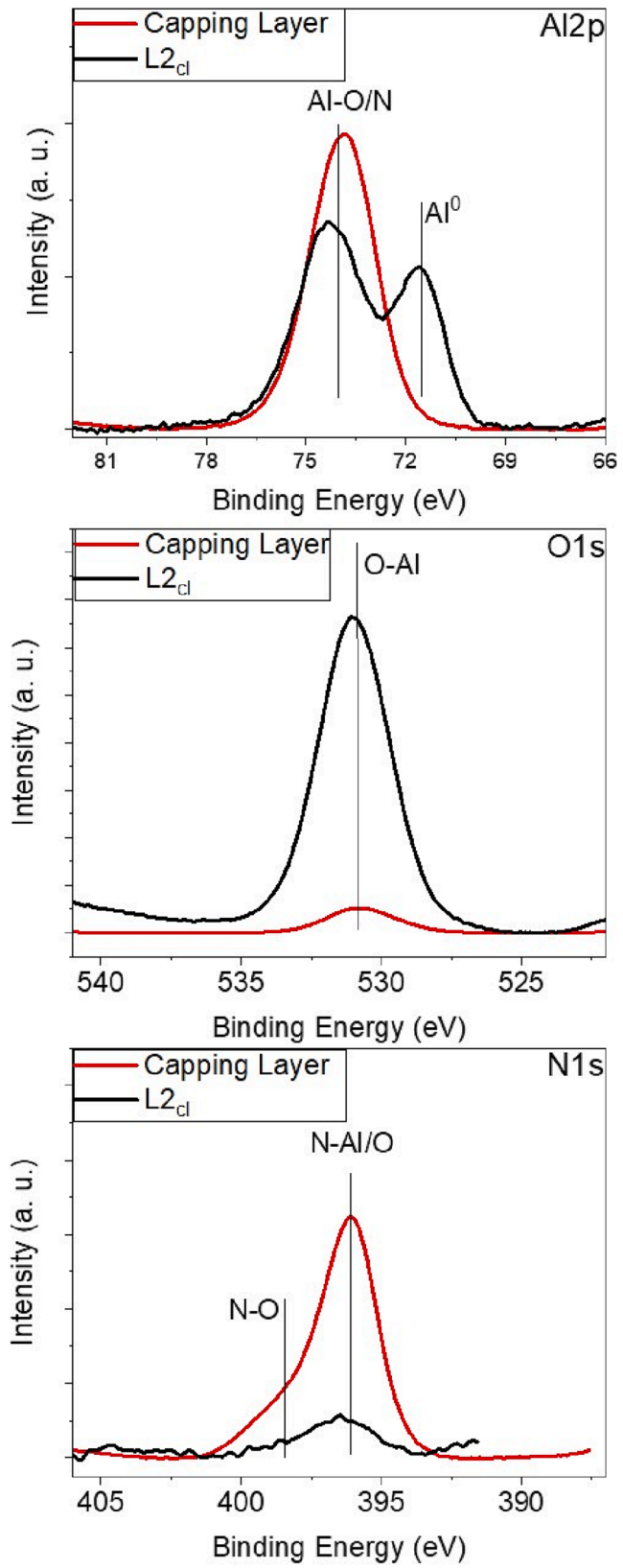

Fig. 4. XPS analysis of the aluminum substrate covered with the aluminum oxynitride layer before and after laser irradiation. The spectra correspond to sample $L2_{cl}$ (see laser irradiation conditions in Table 2). a)-c) signals of Al2p, N1s and O1s photoelectron spectra before and after laser irradiation.

ablation, surface composition corresponds to that an aluminum oxynitride layer (though enriched in oxygen because the exposure of sample to air), where aluminum appears as Al^{3+} (Al 2p BE of 74 eV) and nitrogen as nitride species directly bonded to Al^{3+} or Al^{3+}-$O^{=}$ bonding units (N1s BE at 396.3 eV and 398.5 eV) [42]. After irradiation, Al^{3+} and Al^{0} (BE of 71.5 eV) species characterize the Al2p spectrum, indicating an effective ablation of the capping and outer layers of the samples and a partial oxidation of the generated metal aluminum surface due to its exposure to air (O1s BE at 531.0 eV).

The high effectiveness of the ablation process in samples Ln_{cl} can be tentatively accounted for by the scheme in Fig. 5. According to it, in phase (I), the laser beam becomes absorbed by the Al substrate, passing unmodified through the aluminum oxynitride transparent thin film. During phase (II), the energy of the laser power absorbed by the shallow layers of the aluminum substrate would produce a very effective energization of the aluminum target because temperature would be much higher than in an uncovered Al substrate subjected to a similar laser impact. At this stage the aluminum activated zone would still remain confined within the oxynitride capping layer. In phase (III), the pressure wave generated in the aluminum absorbing zone would induce the removal of the capping layer and the evaporation and ejection of the ablated material from the substrate in the form of a plasma plume. This process would be quite effective thanks to the much high temperatures during the confined substrate activated zones in phases (I) and (II).

3.3. *Wetting and anti-icing properties of ablated surfaces*

The high roughness and surface heterogeneity of Ln_{cl} samples make likely a singular wetting behavior as expected by comparison with other rough and aged metal surfaces [9,18–20,23]. Table 3 and Fig. 6 present and a series of bar diagrams where we compare WCA, hysteresis behavior and freezing delay time of aluminum samples subjected to different laser treatments for the two types of studied samples (i.e., series L1-L4 and $L1_c$-$L4_c$) and their references considered for comparison. Interestingly, an assessment as a function of the actual values of roughness parameters of samples does not provide a direct quantitative correlation between wetting and roughness parameters (see **Fig. S4** in the supporting information section a representation of WCA and hysteresis angles determined for these two series samples as a function of the Sp and Sq parameters, respectively).

Data in Table 3 and Fig. 6 for samples Ln reveal a wetting behavior

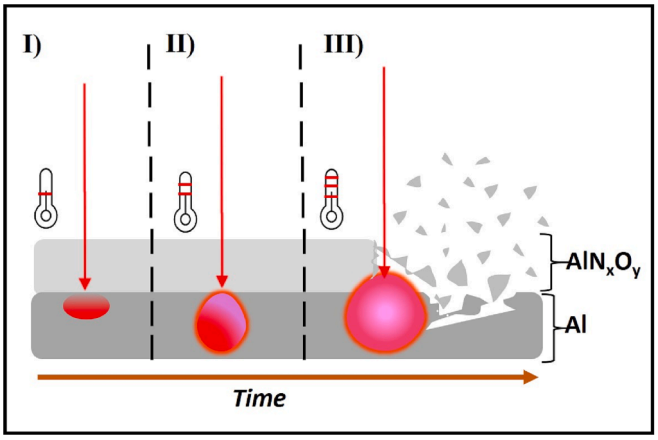

Fig. 5. Scheme of the ablation model accounting for by the roughening of the aluminum surface covered by an aluminum oxynitride capping layer. I) laser beam absorption by the aluminum substrate: heating and melting in a substrate shallow zone confined by the oxynitride layer. II) Temperature increase in the melted zone and formation of a confined plasma; pressure waves push the oxynitride capping layer. III) Eventual removal of the oxynitride capping layer and ablation ejection of aluminum as a high electron temperature plasma plume.

Table 3
Wetting contact angle (WCA), hysteresis contact angle (HA) and freezing delay (FD) time of samples.

Sample	WCA (°)	HCA (°)	FD (min)
S_{Cl}	110 ± 3	22 ± 3	5 ± 1
Al	82 ± 2	35 ± 5	8 ± 2
Al_{Cl}	108 ± 4	10 ± 2	7 ± 2
L1	83 ± 3	33 ± 4	20 ± 4
$L1_{cl}$	131 ± 2	7 ± 2	100 ± 9
L2	72 ± 3	33 ± 5	13 ± 3
$L2_{cl}$	156 ± 2	3 ± 2	82 ± 7
L3	69 ± 4	25 ± 4	11 ± 3
$L3_{cl}$	125 ± 2	4 ± 2	78 ± 6
L4	66 ± 3	29 ± 4	10 ± 4
$L4_{cl}$	159 ± 2	2 ± 1	97 ± 5

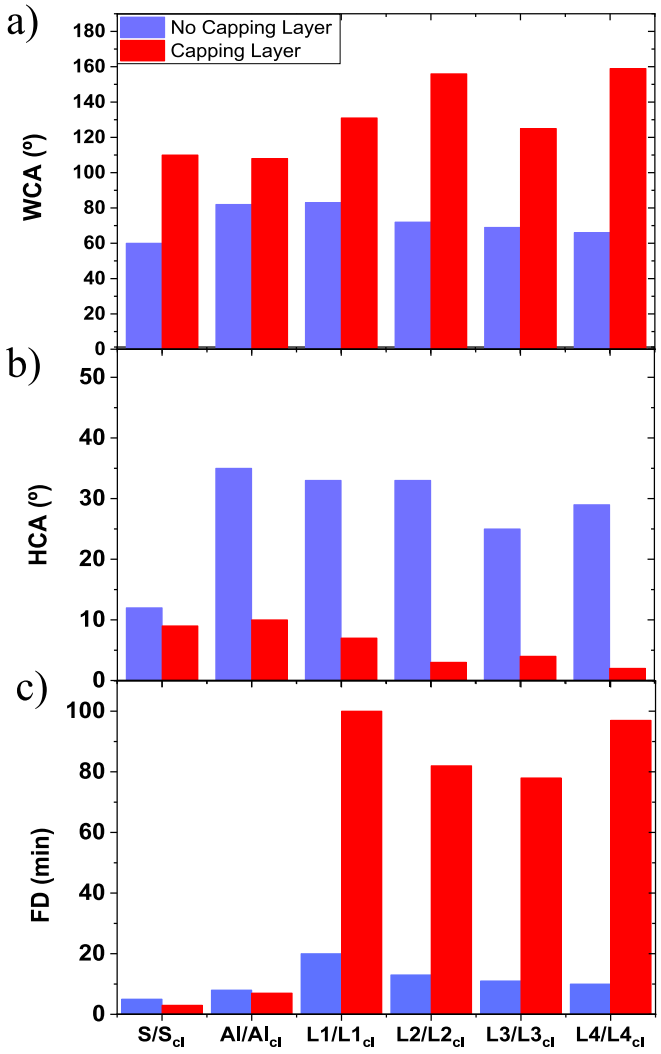

Fig. 6. Bar diagrams for the a) WCAs, b) HCAs and c) FD times determined for the two series of samples L1-L4 and $L1_{cl}$-$L4_{cl}$ prepared by laser ablation of bare and capped aluminum substrates. For comparison data for pristine aluminum and glass substrates are included in the diagrams.

that does not significantly vary with respect to the bare aluminum substrate, characterized by WCA values lower than 90°, hysteresis angles between 30° and 40° and a reduced capacity for rolling-off water droplets on their surface (water droplets remained fixed on the surface even for tilting angles close to 90°). This wetting behavior can be categorized as characteristic of hydrophilic surfaces and is commonly obtained on metal surfaces resulting from laser or other surface activation treatments [4–6,8]. Data reported in Table 3 and Fig. 6 for Ln samples were obtained after one month from the laser treatment, when small WCAs were obtained. This evolution from a highly hydrophilic surface state to less hydrophilic and, sometimes even hydrophobic state has been attributed to surface aging oxidation and contamination with airborne hydrocarbons. The faster transition to a highly hydrophobic or superhydrophobic state in samples Ln_{cl} suggests that their higher values of Sp and Sq parameters and the dual scale character of roughness in these samples make easier the transition to hydrophobicity and stabilizes faster this surface state.

In fact, Fig. 6 shows that the WCA is much higher for Ln_{cl} than for Ln samples, reaching superhydrophobicity for samples $L2_{cl}$ and $L4_{cl}$, characterized for wetting contact angles close to 160 °, a value rarely reported for rough metal surfaces [5–9,19]. Such high WCA values are generally associated with the development of a Cassie-Baxter wetting state resulting from a dual scale roughness at the surface [9]. Sample $L3_{cl}$ also depicts a dual scale roughness, but its long-range heterogeneity (c.f. Fig. 3**c**)) makes this surface less hydrophobic. In this regard, we should highlight that a high value of the roughness parameter Sp or Sq is not sufficient to explain superhydrophobicity and that a dual scale roughness homogeneously distributed over the surface is a requirement for such a wetting behavior. The low value of the hysteresis angle determined for samples Ln_{cl}, particularly $L2_{cl}$ and $L4_{cl}$ (Fig. 6b)), confirms that they posse small surface energies, as desirable for a Cassie Baxter state. It is also noteworthy from the roughness analysis in Figs. 2 and 3 and Table 2, that the values of Sq roughness parameter is almost double for sample $L4_{cl}$ than sample $L2_{cl}$, though both of them were superhydrophobic. We speculate whether, besides the dual scale roughness present in the two cases, the more ordered topography at micron scale found in the latter case (see Fig. 3) might be an additional factor to enhance hydrophobicity as reported for other well ordered structures in the bibliography [37,43].

In agreement with the low hysteresis angles found on samples Ln_{cl}, **rolling**-off angles determined for the superhydrophohbic samples $L2_{cl}$ and $L4_{cl}$ had values of 60°/37°/<2° for droplets volumes of 5, 10 and 15 μL, respectively (see supporting information, **Fig. S5**). This is in good agreement with the measured low hysteresis values, that contrasts with the high rolling-off angles determined for samples Ln, where small droplets of water did not slide even at 90°.

It is also noteworthy that WCA for the superhydrophobic surfaces $L2_{cl}$ and $L4_{cl}$ slightly diminished for increasing Laplace pressure values inside the droplets. An experiment monitoring the WCA as a function of the volume of water droplets letting them evaporate and recording the droplet interaction with the substrate at each state, revealed a decrease from about 151° to 133° in WCA (see **Figs. S6/S7** in the supporting information section**)** for Laplace pressure values of about 100 and 350 Pa, respectively (droplet volume varying from 4 to ca. 0.2 μL). [37,44] This variation, though important, indicate a progressive but limited evolution from a Cassie-Baxter to a Wenzel wetting mode, thus stressing the significant contribution to superhydrophobicity of the dual scale roughness developed in these samples.

Moreover, an aging test consisting of exposing the superhydrophobic samples to a jet of cold water for 3 h in a climatic chamber did not induce any significant change in wetting properties, thus supporting the high stability of these samples against harsh environments (see additional details in the supporting information **S8**).

A high roughness, a Cassie Baxter surface state with a small surface energy and small rolling-off angles constitute a good basis for an effective anti-icing response of metal surfaces (note however that superhydrophobicity is not synonymous of anti-icing behavior [45,46]). A common test to prove the anti-icing capacity of samples is to determine the delay time required for a deposited water droplet to freeze [23–26] (other factors such as ice adhesion, ice accretion capacity or ice sliding easiness are also factors defining the anti-icing character of a surface [47–48]). In this work, we have determined the FD time on the samples Ln and Ln_{cl} prepared by laser ablation. The bar plot presented in Fig. 6**c)**

shows that FD times on samples L1-L4 are short (water freezes in a few minutes after having been cooled at −5°C) and dramatically increases for samples $L1_{cl}$-$L4_{cl}$ up to some hundreds of minutes. Similar FD times have been reported for rough aluminum surfaces modified by a thin Teflon-like layer or functionalized with grafted fluorinated molecules [9,23].

It is also interesting that FD times did not quantitatively correlate with the actual value of the roughness parameters (see **Fig. S9** in the supporting information section), supporting that the existence of a dual scale roughness defining a Cassie Baxter wetting state is the main factor controlling the FD times. According to previous studies on FD of water droplets on the surface of aluminum surfaces, the increase in FD times can be firstly associated with the difficulty to nucleate ice onto surfaces depicting nanometer size porosity, a process requiring surface sites with a size big enough to accommodate the ice nuclei required to initiate the icing process (at −5°C, minimum nucleation size is estimated in 5 nm [9,23,49]). On the other hand, the high thermal conductivity of aluminum would contribute to decrease FD times due to a straightforward release of the heat generated during the water–ice phase transformation [50–52]. Most remarkable from the FD values in Table 3 and Fig. 6**c)** is that they are obtained on bare metal surfaces with just a thin oxide overlayer (see XPS spectra of sample $L2_{cl}$ in Fig. 4**a**)) and therefore with a significant heat transfer capacity. The Cassie Baxter state found in some samples Ln_{cl} characterized by the aforementioned dual scale roughness and air pockets at the surface will partially hinder the heat transmission to the substrate and, in this sense, further contribute to increase the FD times. Taking these freezing factors into account, we associate the long FD times herein determined for samples Ln_{cl}, rather than with the actual value of roughness parameters, to the difficulty to form ice nuclei on the high double scale surface roughness of these samples. It is also noteworthy that FD times at temperatures lower than −5 °C were smaller than the values reported in Table 3, with almost instantaneous freezing for samples Ln and the references, making proper comparative analysis data between Ln and Ln_{cl} samples of little value for discussion.

An additional remark comparing samples Ln and Ln_{cl} is that laser irradiation of aluminum substrates covered with a transparent capping layer does not only induce a higher roughness at relatively low fluences (note for example that sample $L1_{cl}$ does not present a much higher roughness than samples L2 or L4, Table 2) but surely a dual scale roughness combining micro and nanostructures. This is the most effective factor to enhance hydrophobicity and to delay the formation of ice (c.f. Fig. 6). Interestingly, the superhydrophobic state depicted by samples $L2_{cl}$ and $L4_{cl}$ was rather stable upon exposure to a water jet durability test for periods of up to 3 h (see supporting information **S8**). This evidence supports considering these samples for applications where a stable superhydrophobicity is a requirement [53,54]. It is also noteworthy that MS and laser treatment are straightforwardly scalable methods of surface processing and that, therefore, can be applied to treat large surface areas, a significant advantage in comparison with more classical chemical based procedures requiring a more strict control of operating conditions and, not always presenting an easy way to handle the generated subproducts.

4. Conclusions

In the previous results and discussion sections it has been shown that laser irradiation of aluminum substrates capped with a thin and transparent aluminum oxynitride amorphous layer is a suitable strategy to induce an effective ablation process with a NIR laser at relatively low fluences. As a result of this laser irradiation and the ensuing ablation process, the aluminum surface becomes highly rough, free from the covering capping layer and depict outstanding wetting and anti-icing responses that can be modulated playing with the intensity and working conditions of the laser. In concrete, a high superhydrophobicity and long freezing delay times were found for metal aluminum surfaces produced by the proposed capping and laser irradiation procedure. A Cassie Baxter dual scale size state is claimed as responsible for this wetting and freezing behavior.

We stress the important role of the capping layer in favoring the roughening phenomenon as a result of the high temperatures reached in the irradiated zones of the aluminum substrate and the formation of a confined and highly excited state of the metal in the aluminum covered by the transparent oxynitride layer. The final ablation phase, besides removing the oxynitride capping layer, gives rise to a very effective ablation of the aluminum substrate. Final surfaces are much rougher than those generated in the bare aluminum substrates taken as reference.

CRediT authorship contribution statement

Ismail Ghemras: Conceptualization, Data curation, Funding acquisition. **Laura Montes:** Investigation, Data curation, Visualization. **Carmen Lopez-Santos:** Investigation, Visualization, Supervision. **Agustin R. González-Elipe:** Writing – review & editing, Supervision, Funding acquisition. **Victor Rico:** Investigation, Writing – review & editing, Visualization, Supervision, Project administration.

Declaration of Competing Interest

The authors declare that they have no known competing financial interests or personal relationships that could have appeared to influence the work reported in this paper.

Data availability

Data will be made available on request.

Acknowledgements

This work was supported by the General Directorate for Scientific Research and Technological Development (DGRSDT) of the High School Educational and Scientific Research Ministry (MESRS) of Algeria [Grant: P.N.E (2018-2019)]. Also, the project leading to this article has received funding from the EU H2020 program under grant agreement 899352 (FETOPEN-01-2018-2019-2020 - SOUNDofICE). We also thank the AEI-MICINN (PID2019-110430GB-C21, PID2020-112620GBI00 and PID2019-109603RA-I00 funded by MCIN/AEI/10.13039/501100011033 and by "ERDF (FEDER) A way of making Europe," by the "European Union". We acknowledge the financial support of the Consejería de Economía, Conocimiento, Empresas y Universidad de la Junta de Andalucía through the project US-1381045 as well as the EU through cohesion fund and FEDER 2014–2020 programs for financial support. Carmen López-Santos thanks the support of the University of Seville through the VI PPIT-US and the Ramón y Cajal Spanish National programs funded by MCIN/AEI/10.13039/501100011033

Appendix A. Supplementary material

Supplementary data to this article can be found online at https://doi.org/10.1016/j.apsusc.2023.157357.

References

[1] K.-H. Leitz, B. Redlingshoefer, Y. Reg, A. Otto, M. Schmidt, Metal Ablation with Short and Ultrashort Laser Pulses, Phys. Procedia 12 (2011) 230–238, https://doi.org/10.1016/j.phpro.2011.03.128.

[2] B.K. Nayak, M.C. Gupta, Self-organized micro/nano structures in metal surfaces by ultrafast laser irradiation, Opt Lasers Eng 48 (10) (2010) 940–949, https://doi.org/10.1016/j.optlaseng.2010.04.010.

[3] A. Pereira, A. Cros, P. Delaporte, S. Georgiou, A. Manousaki, W. Marine, M. Sentis, Surface nanostructuring of metals by laser irradiation: effects of pulse duration, wavelength and gas atmosphere, Appl. Phys. A 79 (4-6) (2004) 1433–1437.

[4] D.-M. Chun, N. Chi-Vinh, K.-M. Lee, Fast fabrication of superhydrophobic metallic surface using nanosecond laser texturing and low-temperature annealing, CIRP Ann Manuf Technol 65 (1) (2016) 519–522, https://doi.org/10.1016/j.cirp.2016.04.019.

[5] S. Zheng, C. Li, Q. Fu, T. Xiang, W. Hu, J. Wang, S. Ding, P. Liu, Z. Chen, Fabrication of a micro-nanostructured superhydrophobic aluminum surface with excellent corrosion resistance and anti-icing performance, Rsc. Adv. 6 (83) (2016) 79389–79400, https://doi.org/10.1039/c6ra13447e.

[6] R. Jagdheesh, J.J. Garcia-Ballesteros, J.L. Ocana, One-step fabrication of near superhydrophobic aluminum surface by nanosecond laser ablation, Appl. Surf. Sci. 374 (2016) 2–11, https://doi.org/10.1016/j.apsusc.2015.06.104.

[7] L.B. Boinovich, A.M. Emelyanenko, A.D. Modestov, A.G. Domantovsky, K. A. Emelyanenko, Synergistic Effect of Superhydrophobicity and Oxidized Layers on Corrosion Resistance of Aluminum Alloy Surface Textured by Nanosecond Laser Treatment, ACS Appl. Mater. Interfaces 7 (34) (2015) 19500–19508, https://doi.org/10.1021/acsami.5b06217.

[8] Y.K. Cai, W.L. Chang, X. Luo, A.M.L. Sousa, K.H.A. Lau, Y. Qin, Superhydrophobic structures on 316L stainless steel surfaces machined by nanosecond pulsed laser, Precis. Eng. 52 (2018) 266–275, https://doi.org/10.1016/j.precisioneng.2018.01.004.

[9] V.J. Rico, C. Lopez-Santos, M. Villagra, J.P. Espinos, G.F. de la Fuente, L. A. Angurel, A. Borras, A.R. Gonzalez-Elipe, Hydrophobicity, Freezing Delay, and Morphology of Laser-Treated Aluminum Surfaces, Langmuir 35 (19) (2019) 6483–6491, https://doi.org/10.1021/acs.langmuir.9b00457.

[10] A.H.A. Lutey, An improved model for nanosecond pulsed laser ablation of metals, J. Appl. Phys. 114 (8) (2013) pp, https://doi.org/10.1063/1.4818513.

[11] M.A. Jafarabadi, M.H. Mandieh, Investigation of phase explosion in aluminum induced by nanosecond double pulse technique, Appl. Surf. Sci. 346 (2015) 263–269, https://doi.org/10.1016/j.apsusc.2015.03.158.

[12] A. Gragossian, S.H. Tavassoli, B. Shokri, Laser ablation of aluminum from normal evaporation to phase explosion, J. Appl. Phys. 105 (10) (2009), https://doi.org/10.1063/1.3131689.

[13] G. Cristoforetti, S. Legnaioli, V. Palleschi, E. Tognoni, P.A. Benedetti, Observation of different mass removal regimes during the laser ablation of an aluminium target in air, J. Anal. At. Spectrom. 23 (11) (2008) 1518–1528, https://doi.org/10.1039/b800517f.

[14] C. Porneala, D.A. Willis, Observation of nanosecond laser-induced phase explosion in aluminum, Appl. Phys. Lett. 89 (21) (2006), https://doi.org/10.1063/1.2393158.

[15] L.V. Zhigilei, Z. Lin, D.S. Ivanov, Atomistic Modeling of Short Pulse Laser Ablation of Metals: Connections between Melting, Spallation, and Phase Explosion, J. Phys. Chem. C. 113 (27) (2009) 11892–11906, https://doi.org/10.1021/jp902294m.

[16] J. Terragni, A. Miotello, Laser Ablation of Aluminum Near the Critical Regime: A Computational Gas-Dynamical Model with Temperature-Dependent Physical Parameters, Micromachines 12 (3) (2021), https://doi.org/10.3390/mi12030300.

[17] J. Konig, S. Nolte, A. Tunnermann, Plasma evolution during metal ablation with ultrashort laser pulses, Opt. Express. 13 (26) (2005) 10597–10607, https://doi.org/10.1364/opex.13.010597.

[18] A.M. Emelyanenko, F.M. Shagieva, A.G. Domantovsky, L.B. Boinovich, Nanosecond laser micro- and nanotexturing for the design of a superhydrophobic coating robust against long-term contact with water, cavitation, and abrasion, Appl. Surf. Sci. 332 (2015) 513–517, https://doi.org/10.1016/j.apsusc.2015.01.202.

[19] N. Chi-Vinh, D.-M. Chun, Control of laser-ablated aluminum surface wettability to superhydrophobic or superhydrophilic through simple heat treatment or water boiling post-processing, Appl. Surf. Sci. 435 (2018) 974–982, https://doi.org/10.1016/j.apsusc.2017.11.185.

[20] Z. Yang, X. Liu, Y. Tian, Insights into the wettability transition of nanosecond laser ablated surface under ambient air exposure, J. Colloid Interface Sci. 533 (2019) 268–277, https://doi.org/10.1016/j.jcis.2018.08.082.

[21] R.N. Wenzel, Surface roughness and contact angle, J. Phys. Colloid Chem. 53 (9) (1949) 1466–1467, https://doi.org/10.1021/j150474a015.

[22] A.B.D. Cassie, S. Baxter, Wettability of porous surfaces, Trans. Faraday Soc. 40 (1944) 0546–0550, https://doi.org/10.1039/tf9444000546.

[23] V. Rico, J. Mora, P. Garcia, A. Aguero, A. Borras, A.R. Gonzalez-Elipe, C. Lopez-Santos, Robust anti-icing superhydrophobic aluminum alloy surfaces by grafting fluorocarbon molecular chains, Appl. Mater. Today 21 (2020), 100815, https://doi.org/10.1016/j.apmt.2020.100815.

[24] M.A. Sarshar, D. Song, C. Swarctz, J. Lee, C.-H. Choi, Anti-Icing or Deicing: Icephobicities of Superhydrophobic Surfaces with Hierarchical Structures, Langmuir 34 (46) (2018) 13821–13827, https://doi.org/10.1021/acs.langmuir.8b02231.

[25] S. Zhang, J. Huang, Y. Cheng, H. Yang, Z. Chen, Y. Lai, Bioinspired Surfaces with Superwettability for Anti-Icing and Ice-Phobic Application: Concept, Mechanism, and Design, Small 13 (48) (2017) pp, https://doi.org/10.1002/smll.201701867.

[26] P. Tourkine, M. Le Merrer, D. Quere, Delayed Freezing on Water Repellent Materials, Langmuir 25 (13) (2009) 7214–7216, https://doi.org/10.1021/la900929u.

[27] G. Heydari, M.S. Moghaddam, M. Tuominen, M. Fielden, J. Haapanen, J. M. Makela, P.M. Claesson, Wetting hysteresis induced by temperature changes: Supercooled water on hydrophobic surfaces, J. Colloid Interface Sci. 468 (2016) 21–33, https://doi.org/10.1016/j.jcis.2016.01.040.

[28] G. Heydari, E. Thormann, M. Jarn, E. Tyrode, P.M. Caesson, Hydrophobic Surfaces: Topography Effects on Wetting by Supercooled Water and Freezing Delay, J. Phys. Chem. C. 117 (42) (2013) 21752–21762, https://doi.org/10.1021/jp404396m.

[29] S. Jung, M.K. Tiwari, N.V. Doan, D. Poulikakos, Mechanism of supercooled droplet freezing on surfaces, Nat. Commun. 3 (2012) pp, https://doi.org/10.1038/ncomms1630.

[30] A. Belosludtsev, J. Vlcek, J. Houska, S. Haviar, R. Cerstvy, Tunable composition and properties of Al-O-N films prepared by reactive deep oscillation magnetron sputtering, Surf. Coat. Technol. 392 (2020) pp, https://doi.org/10.1016/j.surfcoat.2020.125716.

[31] J. Borges, N. Martin, N.P. Barradas, E. Alves, D. Eyidi, M.F. Beaufort, J.P. Riviere, F. Vaz, L. Marques, Electrical properties of AlNxOy thin films prepared by reactive magnetron sputtering, Thin Solid Films 520 (21) (2012) 6709–6717, https://doi.org/10.1016/j.tsf.2012.06.062.

[32] J. Borges, F. Vaz, L. Marques, AlNxOy thin films deposited by DC reactive magnetron sputtering, Appl. Surf. Sci. 257 (5) (2010) 1478–1483, https://doi.org/10.1016/j.apsusc.2010.08.076.

[33] Y.-H. Lin, J.-C. Hsu, Y. Ding, P.W. Wang, Optical properties of high transmittance aluminum oxynitride thin films for spectral range from near ultraviolet to visible, Opt. Rev. 16 (3) (2009) 400–403, https://doi.org/10.1007/s10043-009-0076-6.

[34] K.A. Aissa, A. Achour, O. Elmazria, Q. Simon, M. Elhosni, P. Boulet, S. Robert, M. A. Djouadi, AlN films deposited by dc magnetron sputtering and high power impulse magnetron sputtering for SAW applications, J Phys D Appl Phys 48 (14) (2015), https://doi.org/10.1088/0022-3727/48/14/145307.

[35] F.M. Mwema, E.T. Akinlabi, O.P. Oladijo, A systematic review of magnetron sputtering of AlN thin films for extreme condition sensing, Mater. Today: Proc. 26 (2020) 1546–1550, https://doi.org/10.1016/j.matpr.2020.02.317.

[36] B. Riah, A. Ayad, J. Camus, M. Rammal, F. Boukari, L. Chekour, M.A. Djouadi, N. Rouag, Textured hexagonal and cubic phases of AlN films deposited on Si (100) by DC magnetron sputtering and high power impulse magnetron sputtering, Thin Solid Films 655 (2018) 34–40, https://doi.org/10.1016/j.tsf.2018.03.076.

[37] R. Pan, M. Cai, W. Liu, X. Luo, C. Chen, H. Zhang, M. Zhong, Extremely high Cassie-Baxter state stability of superhydrophobic surfaces via precisely tunable dual-scale and triple-scale micro–nano structures, J. Mater Chem. A 7 (2019) 18050, https://doi.org/10.1039/c9ta04484a.

[38] A. Wexler, Vapor-pressure formulation for ice, J. Res. Nat. Bur. Stand. Sect. A-Phys. Chem. 81 (1) (1977) 5–20, https://doi.org/10.6028/jres.081A.003.

[39] X. Guo, C.-L. Zou, H.X. Tang, Second-harmonic generation in aluminum nitride microrings with 2500%/W conversion efficiency, Optica 3 (10) (2016) 1126–1131, https://doi.org/10.1364/optica.3.001126.

[40] C. Xiong, W.H.P. Pernice, C. Schuck, H.X. Tang, Ieee, Second harmonic generation in aluminum nitride waveguides on silicon substrates, Conference on Lasers and Electro-Optics (CLEO), San Jose, CA, 2012.

[41] V. Yoshioka, J. Lu, Z. Tang, J. Jin, R.H. Olsson, B. Zhen, Strongly enhanced second-order optical nonlinearity in CMOS-compatible Al1-xScxN thin films, Apl. Mater. 9 (10) (2021) pp, https://doi.org/10.1063/5.0061787.

[42] D. Cao, X. Cheng, Y.-H. Xie, L.i. Zheng, Z. Wang, X. Yu, J. Wang, D. Shen, Y. Yu, Yu, Effects of rapid thermal annealing on the properties of AlN films deposited by PEALD on AlGaN/GaN heterostructures, Rsc Adv. 5 (47) (2015) 37881–37886.

[43] K.L. Wilke, Y. Song, Z. Lu, E.N. Wang, Enhanced Laplace Pressures for Functional Surfaces: Wicking, Switchability, and Selectivity, Adv Materials Inter 10 (4) (2023) 2201967.

[44] A.K. Gnanappa, D.P. Papageorgiou, E. Gogolides, A. Tserepi, A.G. Papathanasiou, A.G. Boudouvis, Hierarchical, Plasma Nanotextured, Robust Superamphiphobic Polymeric Surfaces Structurally Stabilized Through a Wetting– drying Cyclea, Plasma Proc. Polym. 9 (3) (2012) 304–315.

[45] M.I. Jamil, A. Ali, F. Haq, Q. Zhang, X. Zhan, F. Chen, Icephobic Strategies and Materials with Superwettability: Design Principles and Mechanism, Langmuir 34 (50) (2018) 15425–15444, https://doi.org/10.1021/acs.langmuir.8b03276.

[46] S.S. Latthe, R.S. Sutar, A.K. Bhosale, S. Nagappan, C.-S. Ha, K.K. Sadasivuni, S. Liu, R., Xing, Recent developments in air-trapped superhydrophobic and liquid-infused slippery surfaces for anti-icing application, Prog. Org. Coat. 137 (2019), https://doi.org/10.1016/j.porgcoat.2019.105373.

[47] P.F. Ibanez-Ibanez, F.J.M. Ruiz-Cabello, M.A. Cabrerizo-Vilchez, M.A. Rodriguez-Valverde, Ice adhesion of PDMS surfaces with balanced elastic and water-repellent properties, J. Colloid Interface Sci. 608 (2022) 792–799, https://doi.org/10.1016/j.jcis.2021.10.005.

[48] A.J. Meuler, J.D. Smith, K.K. Varanasi, J.M. Mabry, G.H. McKinley, R.E. Cohen, Relationships between Water Wettability and Ice Adhesion, ACS Appl. Mater. Interfaces 2 (11) (2010) 3100–3110, https://doi.org/10.1021/am1006035.

[49] N.H. Fletcher, Size effect in heterogeneous nucleation, J. Chem. Phys. 29 (3) (1958) 572–576, https://doi.org/10.1063/1.1744540.

[50] A. Alizadeh, M. Yamada, R. Li, W. Shang, S. Otta, S. Zhong, L. Ge, A. Dhinojwala, K. R. Conway, V. Bahadur, A.J. Vinciquerra, B. Stephens, M.L. Blohm, Dynamics of Ice Nucleation on Water Repellent Surfaces, Langmuir 28 (6) (2012) 3180–3186, https://doi.org/10.1021/la2045256.

[51] P. Guo, Y. Zheng, M. Wen, C. Song, Y. Lin, L. Jiang, Icephobic/Anti-Icing Properties of Micro/Nanostructured Surfaces, Adv. Mater. 24 (19) (2012) 2642–2648, https://doi.org/10.1002/adma.201104412.

[52] F.J. Montes Ruiz-Cabello, S. Bermudez-Romero, P.F. Ibanez-Ibanez, M. A. Cabrerizo-Vilchez, M.A. Rodriguez-Valverde, Freezing delay of sessile drops: Probing the impact of contact angle, surface roughness and thermal conductivity, Appl. Surf. Sci. 537 (2021), https://doi.org/10.1016/j.apsusc.2020.147964.

[53] I. Malavasi, I. Bernagozzi, C. Antonini, M. Marengo, Assessing durability of superhydrophobic surfaces, Surf. Innov. 3 (1) (2015) 49–60, https://doi.org/10.1680/si.14.00001.

[54] D. Wang, Q. Sun, M.J. Hokkanen, C. Zhang, F.Y. Lin, Q. Liu, S.P. Zhu, T. Zhou, Q. Chang, B. He, Q. Zhou, L. Chen, Z. Wang, R.H.A. Ras, X. Deng, Design of robust

superhydrophobic surfaces, Nature 582 (7810) (2020) 55–59, https://doi.org/10.1038/s41586-020-2331-8.